3D Particle Tracking Velocimetry using Synthetic Aperture Imaging

by

Abhishek Bajpayee

B.S., University of Louisiana at Lafayette (2008)

Submitted to the Department of Mechanical Engineering
in partial fulfillment of the requirements for the degree of

Master of Science in Mechanical Engineering

at the

MASSACHUSETTS INSTITUTE OF TECHNOLOGY

February 2014

Author .....
Department of Mechanical Engineering
January 17, 2014

Certified by .....
Alexandra H. Techet
Associate Professor of Mechanical and Ocean Engineering
Thesis Supervisor

Accepted by .....
David Hardt
Ralph E. and Eloise F. Cross Professor of Mechanical Engineering
Chairman, Department Committee on Graduate Theses

3D Particle Tracking Velocimetry using Synthetic Aperture Imaging

by

Abhishek Bajpayee

Submitted to the Department of Mechanical Engineering
on January 17, 2014, in partial fulfillment of the
requirements for the degree of
Master of Science in Mechanical Engineering

Abstract

3D visualization of fluid flow is of critical significance to a number of applications ranging from micro-scale medical devices to design of ships and airplanes. Of the various techniques currently used to visualize flow fields, particle image velocimetry (PIV) offers great advantages because of the high resolution quantitative results it provides. The feasibility of using synthetic aperture (SA) imaging to conduct 3D Particle Image Velocimetry (PIV) has been previously demonstrated. This thesis presents the development of a technique that extends SA imaging to 3D Particle Tracking Velocimetry (PTV), adding the ability to conduct Lagrangian studies on flow fields over time.

A new method has been developed to accurately locate seeding particles in volumes reconstructed using SA imaging, based on a proposed thresholding and average intensity based scheme, which is able to locate particles in densely seeded flows. In addition, a new and much faster method for reconstructing volumes, based on a homography fit (HF) refocusing method, is proposed which facilitates rapid processing of large amounts of data recorded using high speed cameras for example. The capability of using SA imaging to conduct PTV is demonstrated by tracking located particles using the relaxation based algorithm.

The developed technique provides accurate and high resolution PTV results at a much higher computation speed compared to other state of the art techniques. If engineered further,the presented technique has the potential to become the method of choice to conduct velocimetry.

Thesis Supervisor: Alexandra H. Techet
Title: Associate Professor of Mechanical and Ocean Engineering

Acknowledgments

This thesis and the work presented herein is a cumulative result of events in my life that were affected by certain individuals. Without the help, support and vision of these people the completion of this work would not have been possible.

I am extremely thankful to my adviser Alexandra Techet, who has provided me with critical support and guidance without which none of this work would have been possible. In addition, I am thankful to other members of the Experimental Hydrodynamics Lab, Leah Mendelson and Barry Scharfman who helped with experiments and discussions.

I will always be eternally thankful to my parents, Dinesh Kumar Bajpayee and Neelu Bajpayee. They have always provided me with the resources, support, values and love that I most needed to reach the point in life where I am. I would like to dedicate this thesis to them, for I am at MIT because of their vision and sacrifice.

I am also thankful to my aunt and uncle, Sunita and Rakesh Bapjai, who have always been like second parents. Their love, support, and advice through my college years have played a significant role in shaping who I am today.

I am equally thankful to my brother Anurag Bajpayee, who has been a guide and mentor, an idol, a constant source of inspiration, a friend and much more than a brother can ever be. His advice, motivation, and support have always been extremely valuable to me. I am also thankful to my sister-in-law, Ambika Goel Bajpayee, for her love, support and advice.

I would also like to acknowledge my former adviser at MIT, Alexander Mitsos, for his support for my admission to MIT and throughout my first year as a graduate student.

Last but not the least, I am thankful to my friends here at MIT - Sudeep Pillai, Carl Vondrick, Shreya Saxena, Yekaterina Tarasova, and Ashwin Raghavan. They have been great companions, source of emotional support, and have been helpful both in research and otherwise.

THIS PAGE INTENTIONALLY LEFT BLANK

Contents

List of Figures

THIS PAGE INTENTIONALLY LEFT BLANK

List of Tables

THIS PAGE INTENTIONALLY LEFT BLANK

Chapter 1

Introduction

1.1 Motivation

Given the unsteady three dimensional nature of fluid flows encountered in both research and industry, there is a high demand for advanced experimental techniques that fully resolve velocity fields in time and space. Velocimetry techniques have evolved from being based on pitot-static tubes, hot-wire anemometry and laser doppler anemometry ([12], [9], and [1]) to 2D Particle Image Velocimetry (PIV) [2]. In recent years, 3D velocimetry techniques such as tomographic PIV [11], holographic PIV [28] and digital defocusing PIV [24] have been developed. Additionally, concepts from the light field imaging community have been developed into 3D PIV codes with great promise for fast calculation of complex unsteady velocity fields. This thesis outlines the extension of light field imaging concepts, particularly those of synthetic aperture (SA) imaging, to particle tracking.

The most widely used 3D PIV technique is tomographic PIV. Tomographic PIV, pioneered by Elsinga et al [11], has gained significant popularity since first proposed in 2006. This technique relies on images from about 4 or 5 cameras looking at a scene from different viewpoints to facilitate tomographic reconstruction of the investigation volume using an algebraic reconstruction technique (ART) or a multiplicative algebraic reconstruction technique (MART). Atkinson et al [3] identified that the MART algorithm, which was standard at that time, was expensive both computa-

tionally and in terms of memory requirements; proposed improvements and reported a gain in computation speed of over 70 times. Novara et al [20] proposed a motion tracking enhanced (MTE) MART tomographic reconstruction technique and reported improvements in reconstruction accuracy. Recently, time resolved tomographic PIV was used by Schroder et al [27] to study a turbulent boundary layer and by Violato et al [29] to calculate the pressure field of a rod-airfoil flow to good accuracy. Kitzhofer et al [17], Doh et al [10] and Novara et al [21] have recently demonstrated the ability of tomographic reconstructions to be used for PTV purposes. Other techniques such as holographic PIV and digital defocusing PIV are not as popular as tomographic PIV (which is already being commercialized) and tomographic PIV stands out in terms of accuracy, resolution and allowed size of investigation volume.

Hain et al [13] reported in 2008 that the time taken to reconstruct a single $3512 \times 2562 \times 599$ voxel volume, using four MART iterations, was about 34 hrs on a dual core computer. Time taken to cross correlate volumes in order to calculate velocity vectors was an additional 100 hrs. It must be noted that this performance is prohibitive towards processing of time resolved data, especially high speed, because processing a time sequence of 30 frames at the same resolution, based on aforementioned reported results, would take 42 days! Even though CPU performance has greatly improved since 2008 the speed of such an algorithm will still be slow. It is thus desirable to have a technique that can achieve the same resolution and accuracy as tomographic PIV but in a shorter computational time. The relevance of this issue will be addressed in Section 2.4 of this thesis.

The novel application of Synthetic Aperture (SA) imaging to 3D PIV and for bubble identification in Multi Phase flows was demonstrated by Belden et al in [8] and [7] respectively. They utilized the fact that SA imaging allows one to focus at any arbitrary depth in a volume of interest to reconstruct accurate intensity volumes to be used for 3D cross correlation based PIV. This application was identified to have several advantages as a fluid flow imaging technique. It allowed an out of plane resolvable (Z) dimension of the same order as the in plane (X-Y) dimension and facilitated seeing through some occlusions in the scene thus increasing spatial resolvability of

particles/features. It also performed better than most other technologies with densely seeded flows. Belden et al [8] used an array of up to 10 cameras that recorded at a maximum of 30 frames per second and were able to demonstrate the ability to spatially resolve densely seeded velocity fields with great accuracy.

PIV, even when performed over time, only provides Eulerian information about the flow and does not provide individual particle trajectories. This restricts one from performing studies, analysis of fluid mixing for example, which require Lagrangian information about the flow field. Additionally, since PIV techniques use a finite sized window to cross correlate images or volumes, existing techniques can be limited in terms of spatial resolution and often do not resolve small scale flow features.

In order to develop a velocimetry technique capable of providing Lagrangian particle trajectories, this thesis investigates the applicability of SA imaging to 3D PTV. A new thresholding and average intensity based particle search scheme is proposed, which on a 2D level is based on a particle detection technique similar to dynamic threshold binarization proposed by Ohmi et al [23], but is extended and further developed to facilitate accurate 3D localization of particles in the observation volume. The particles once located in space can then be tracked using several methods such as nearest neighbor, neural networks, the relaxation method, variational method etc. depending on seeding density and average velocity in the tracking region. For the purpose of this study, the relaxation method was used.

1.2 Synthetic Aperture Imaging

Synthetic Aperture (SA) imaging is a technique that projects images of the same scene shot from different cameras (different view points) onto a virtual focal plane. Essentially, SA imaging simulates images captured via a lens of an arbitrary sized aperture. It is commonly observed that large aperture lenses, such as those used on DSLR cameras, have a shallow depth of field. Cameras with smaller apertures however, a cellphone camera for example, have a much larger depth of field. In principle, as the aperture size of a lens increases its depth of field becomes smaller. Figure 1-1

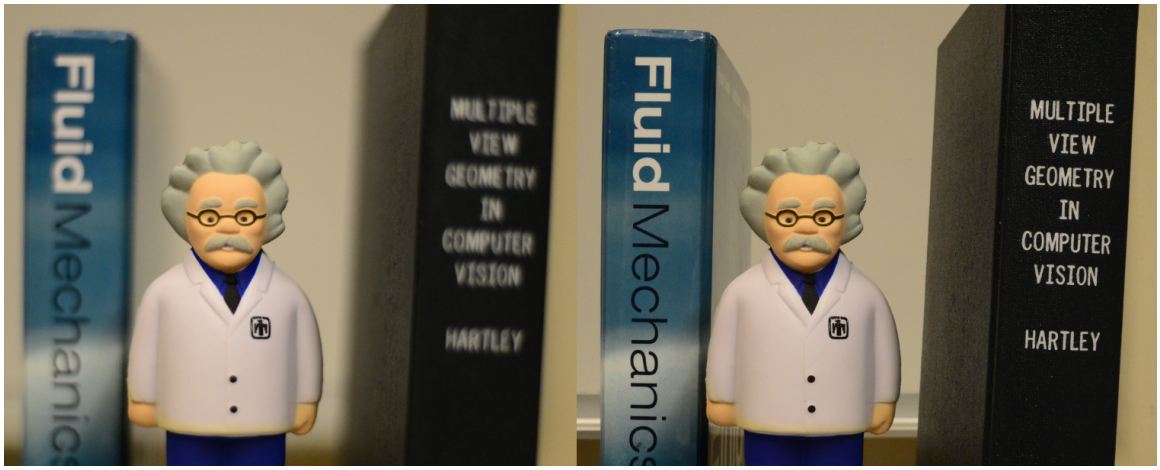

Figure 1-1: Images of the same scene shot using different aperture sizes. The image on the left was shot using an aperture size of f1.8 and the one on the right was shot using an aperture of f22 using a Nikkor 50mm lens.

shows two images of the same scene captured using different sized apertures. It can clearly be seen that a larger aperture (smaller f number) has a smaller depth of field. SA imaging allows one to simulate a lens with a much larger aperture using multiple cameras looking at the same scene from slightly different viewpoints. Figure 1-2 shows a schematic for a typical camera array for SA imaging purposes. By combining images from each camera in such an array using principles of SA imaging, one can calculate an image sharply focused at an arbitrary depth in the scene. The apparent depth of field in such an image is a function of the spacing between cameras and distance of array from scene i.e. dx, dy and D. If dx and dy were equal, the effective aperture radius of such an array would be $dx\sqrt{2}$.

1.2.1 Application to 3D PIV and PTV

By increasing the distance between cameras, the depth of field of such an array can be reduced sufficiently such that it can be used to image particles in a flow field essentially lying on the focal plane of the calculated images. Particles away from the focal plane are significantly blurred and can be removed, thus allowing one to reconstruct the entire volume of interest, in a particle laden tank. This reconstructed volume can then be used to conduct PIV in 3D, as shown by Belden [8]. In this

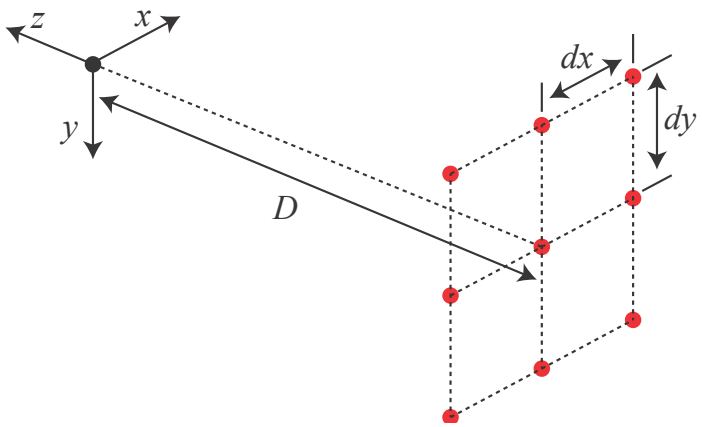

Figure 1-2: Schematic for a typical camera array for SA imaging purposes. Red dots indicate locations of cameras all looking at the origin.

study, it was observed that the reconstructed volumes using SA imaging were not only feasible for conducting cross correlation based PIV but could also be used to locate individual seeding particles in space. Discrete particle locations could then be tracked over time to conduct PTV.

This thesis describes, in detail, the techniques that were developed in order to rapidly reconstruct intensity volumes of particle laden flow fields, accurately calculate particle locations from them, and track these located particles over time. Improvements in volume reconstruction speed facilitate processing of data captured using high speed cameras.

THIS PAGE INTENTIONALLY LEFT BLANK

Chapter 2

Synthetic Aperture Refocusing

Principles of synthetic aperture imaging are used to calculate images, using recorded data, that are sharply focused at an arbitrary depth in the scene spanning the entire volume of interest. This is achieved by back projecting images from each camera to calculate images at a given depth followed by merging of these images to calculate the refocused image. This process will be henceforth referred to as SA Refocusing. Pinhole SA refocusing, outlined in section 2.2.1, is fairly simple and computationally cheap but can only be used if the scene does not contain any refractive interfaces (such as those in a scene with a water tank). However, if the scene does contain refractive interfaces, which is the case in all experiments, refractive SA refocusing (outlined in section 2.2.2) must be used which takes into account the bending of light rays due to refraction at each interface to back project images. This chapter will discuss both pinhole and refractive SA refocusing methods that have been used in this study.

Time taken to calculate SA refocused images is directly proportional to the time taken to back project a single pixel. Each pixel in each image from all cameras in the array is back projected to calculate an image refocused at a given depth. This is repeated to calculate images at multiple depths, a small distance apart, spanning the entire volume of investigation. The significance of this fact will be addressed later in this chapter where a new refractive SA refocusing method is presented to greatly improve computation speed.

2.1 Calibration

Before specifics of the refocusing methods can be discussed, a few details about the calibration process must be presented. Most cameras can be approximated using a pinhole camera model according to which any point p_i in the scene can be projected to an image u_{ij} in the j^{th} camera using a camera matrix P_j using the following relation:

$$u_{ij} = P_j p_i \tag{2.1}$$

$$P_j = K_j[R_j|t_j] \tag{2.2}$$

where P_j is a 4x3 matrix called the camera matrix and is calculated using K_j, R_j and t_j which are the j^{th} camera's intrinsic parameter matrix, rotation matrix and translation matrix respectively. Camera models are discussed in extensive detail by Hartley et al [14].

Cameras, looking at the same scene, can be calibrated using a bundle adjustment optimization scheme by recording images of a chessboard pattern[1] of known physical size. A bundle adjustment optimization scheme minimizes the total reprojection error of all points (which in this case are the detected corners of a chessboard pattern) and can be written as:

$$min \sum_j \sum_i d(Q(P_j, p_i), x_{ij}) \tag{2.3}$$

where x_{ij} is location of point p_i in image in the j^{th} camera and $d(x, y)$ is the euclidian distance between point x and y. The function Q projects the 3D point p_i into a camera with camera matrix P_j. For a scene with no refractive interfaces, this function is same as Eqn. 2.1 but for a scene with refractive interfaces in it this function must take refraction into account. In this context this function first projects point p_i to

[1]Other objects (3D or planar) can also be used that have machine recognizable features arranged in a known geometric pattern.

point a_i, through water and glass to front wall of tank, solving Snell's law and then projects a_i into a camera using Equation 2.1. This method and the experimental intricacies involved in the calibration process are outlined in detail by Belden [6]. This projection process involves an iterative step, solved using the Newton Raphson method, to ensure that Snell's law is satisfied.

The calibration process yields the K, R and t matrices for each camera and the 3D coordinates of all points p_i. For cases with refractive interfaces it also yields the depth at which the glass wall of the tank is located in the scene. The thickness of glass wall and refracive indices of glass and water are assumed constant. These parameters can later be used to back project images to calculate refocused images.

2.2 Refocusing Methods

2.2.1 Pinhole Refocusing

A point u_{ij} projected into a camera can be back projected to a 3D point using the pseudoinverse P^+ of the camera matrix. Each image I_j, from j^{th} camera, is back projected to depth z (in world coordinates) to a set of points B_j^z. These points can then be used to form an image I_j^z by transforming the x and y coordinates in B_j^z, which are in world units, to pixel units using the following relation:

$$I_j^z = DB_j^z \tag{2.4}$$

where the matrix D has the form

$$D = \begin{bmatrix} \alpha_x & 0 & c_x \\ 0 & \alpha_y & c_y \\ 0 & 0 & 1 \end{bmatrix} \tag{2.5}$$

and α_x and α_y are factors that convert world coordinates to pixels coordinates and c_x and c_y are coordinates of the principal point of the image. The back projected images from each camera can then be combined using either an additive method:

$$I_z = \frac{1}{N}\sum_j I_j^z \tag{2.6}$$

or a multiplicative method:

$$I_z = \prod_j (I_j^z)^\alpha \tag{2.7}$$

where I_z is the calculated image focused at depth z, N is a the number of cameras in the array and α is a power each back projected image is raised to and its value generally is the inverse of the number of cameras $1/N$. Combinations of additive and multiplicative methods can also be used. The additive method was primarily used in this study. It must be mentioned that α can have different values depending on the desired effect on pixel intensities.

2.2.2 Refractive Refocusing

In the presence of refractive interfaces in the scene, the effect of refraction must be taken into account when back projecting an image to a given depth. To calculate this back projected image, an assumed image I_j^z is projected into the j^{th} camera through the water and glass to an image R_j^z using the same method that is used to project a 3D point into a camera during the calibration process. Note that the first step in this process will involve conversion of I_j^z to B_j^z from pixel units to world units using the inverse of Eqn. 2.4. Points in R_j^z are then used to calculate an inverse mapping function using which an image I_j is warped to a back projected image I_j^z. These back projected images can then be combined using Equations 2.6 and 2.7.

2.2.3 Fast Refractive Refocusing: Homography Fit (HF) Method

For experimental cases, the most computationally time consuming step in the entire PTV process is the refocusing step. This is because back projection for refractive refocusing takes much longer than pinhole back projection because it requires multiple iterations for each pixel. Thus, if one hopes to process data recorded using high speed cameras, refocusing speed must be greatly improved.

Any imperfections in the glass wall of the tank are neglected and the wall is assumed to be perfectly flat and of a given thickness and thus all light rays are being refracted at planar interfaces. For a simple pinhole camera, the back projection process can be reduced to a homography transform since points in one image are mapped to another such that straight lines remain straight (basic property of projective transforms in the absence of distortion). It can be shown that collinear 3D points when refracted through planar interfaces and then projected into a pinhole camera remain collinear in the image. As a result, the projection of 3D points into a camera through planar refractive interfaces can be approximated with a simple projective transform. The back projection step can thus be achieved by approximating the required inverse mapping function by a simple homography transform, as in the case of pinhole back projection. A homography matrix H for this approximation can be computed using a minimum of 4 non collinear points in the projected image R_j^z as shown in Figure 2-1. This matrix H can then be used to calculate a back projected image in the following manner:

$$I_j^z = HI_j \tag{2.8}$$

This Homography Fit (HF) method reduces the computational cost by several orders of magnitude as now only 4 points have to be projected through refractive interfaces compared to as many points as the number of pixels in the images being used.

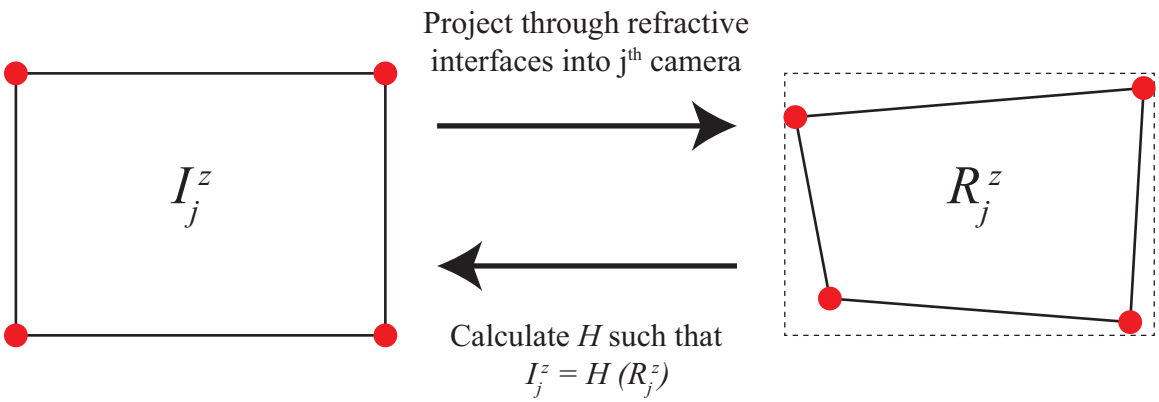

Figure 2-1: Estimation of H in Homography Fit method

2.3 Validation of the HF Method

In order to validate the HF method, the reconstruction quality Q of intensity fields reconstructed using this method was compared to that of intensity fields reconstructed using the original refractive refocusing method. The reconstruction quality Q here is:

$$Q = \frac{\sum_{X,Y,Z} E_r(X,Y,Z) \cdot E_s(X,Y,Z)}{\sqrt{\sum_{X,Y,Z} E_r^2(X,Y,Z) \cdot \sum_{X,Y,Z} E_s^2(X,Y,Z)}} \tag{2.9}$$

where is the E_r is reconstructed intensity field and E_s is the synthesized intensity volume. Figure 2-2 shows a comparision between reconstruction quality obtained from both methods as it changes with number of seeded particles in synthetic volume and threshold level T which is the intensity (on a scale of 0 to 255) below which a pixel intensity is set to zero. Thresholding removes the discrete blur, an inherent characteristic of SA refocused images. The discrete blur if discussed in detail in Chapter 3.

It can be seen that the reconstruction quality of intensity fields obtained using the HF method is slightly less than that of intensity fields obtained using the original method. Q decreases for both methods as seeding density increases because of increase in noise due to blurred particles that are not removed. Also Q increases with increase in T initially because of decreased visible blurred particles and eventually decreases

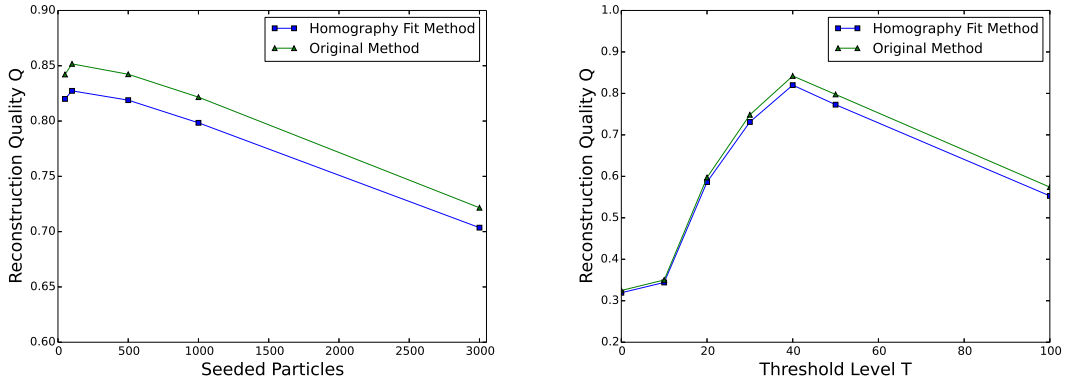

(a) Q vs seeded particles for both methods for $T = 40$

(b) Q vs threshold level T for both methods for 1000 seeded particles

Figure 2-2: A comparison of reconstruction quality obtained from HF and original refocusing methods as it changes with number of seeded particles and threshold level T.

again due to decrease in z extent of particles. It will be shown in Chapter 3 that this decrease in Q when using the HF method can be traded for computation speed without any significant loss in accuracy.

2.4 Relevance to High Speed Imaging

As mentioned in Section 2.2.3, refocusing the images using the original method takes a long time and the refocusing step accounts for most of the processing time taken by the entire PTV process. This drawback was identified as a significant hurdle to processing large amounts of data especially that acquired using high speed cameras. As a result the code developed for this study was written to run on CUDA capable GPUs. Table 2.1 lists code benchmarking results, on different machines with and without using a GPU, based on calculating refocused images 0.1 mm dz apart for one time step for a volume 110 mm in size in the z direction ($1280 \times 800 \times 1100$ voxels). Note that this step is performed for multiple consecutive frames in a sequence of recorded data to calculate particle locations that can be then tracked.

The timing results shown can be explained based on the difference in CPU clock speeds and the GPUs onboard each machine. Performance on the desktop when

using only CPU is better on account of the higher clock speed since the code is not CPU parallelized. It can be seen that using a GPU drastically improves performance. Using the HF method to refocus images further improves performance resulting in processing times up to 3 orders of magnitude lesser. To consider an example, during experiments conducted during this study, several data sets were recorded using high speed cameras, in each of which at least 50 frames were of interest. The size of the investigation volume in the z direction was about 40 mm. Based on timing results shown, processing only one such data set would take about 14 hours on a typical lab desktop computer with a modest GPU. Note that this does not take into account additional time taken by the particle localization step. Moreover, it would take even longer to process on a computer without a GPU. In contrast, processing the same amount of data on the same computer using the HF method would take about 115 seconds. Thus the HF method leads to more than 400 times the speed and facilitates processing of large amounts of high speed data in a reasonable amount of time.

These results are also compared with timing results for tomographic PIV as reported in literature. In 2008, Hain et al [13] reported that the time taken to reconstruct a single $3512 \times 2562 \times 599$ voxel volume, using 4 MART iterations, was about 34 hrs on a dual core computer. This averages to about 22.72 μs per voxel. In 2009, Atkinson et al [3] reported a 65 fold increase in performance over that reported by Hain et al. This averages to about 0.35 μs per voxel. These per voxel times were used to estimate how much time these methods would take to reconstruct a volume $1280 \times 800 \times 1100$ voxels in size. Table 2.2 compares the peak performance of the code developed and used in this study with the estimated tomographic reconstruction performance. The best case (Desktop + GPU using the HF method) translates to a 60 fold improvement on the method used by Atkinson et al. It is acknowledged that the results reported by Hain et al and Atkinson et al are from 2008 and 2009 respectively and might perform better on newer CPUs. However, this improvement is unlikely to be large enough to bridge a 60 fold gap.

Table 2.1: Time taken to reconstruct a $1280 \times 800 \times 1100$ voxels volume. Desktop specifications: Intel Core i7 CPU clocked at 2.93 GHz with an NVIDIA GeForce GTX 650 Ti GPU (768 CUDA cores), Server specifications: Intel Xeon CPU clocked at 2.6 GHz with an NVIDIA Tesla K20c GPU (2496 CUDA cores).

	HF Method	Original Method
Desktop	88 s	168 min
Server	105 s	182 min
Desktop + GPU	6.31 s	46.1 min
Server + GPU	4.11 s	6.38 min

Table 2.2: Time taken to reconstruct a $1280 \times 800 \times 1100$ voxels volume. Desktop specifications same as mentioned in Table 2.1

	Time
Desktop (using HF method)	88 s
Desktop + GPU (using HF method)	6.31 s
Reported by Hain et al	7 hrs
Reported by Atkinson et al	6.5 min

THIS PAGE INTENTIONALLY LEFT BLANK

Chapter 3

Particle Localization

PIV relies on cross correlation of greyscale intensity images or 3D intensity volumes in order to calculate local flow velocity. However, PTV requires discrete particle locations in space so that they can be tracked over time. As a result, a technique that would calculate 3D locations of individual particles from SA refocused images had to be developed. This involves a combination of preprocessing of images to accentuate particles and remove noise, actual localization of particles (or local intensity peaks) in images, followed by inference of their 3D location. This chapter outlines the developed particle localization scheme in detail.

3.1 Preprocessing

3.1.1 Discrete Blur

As outlined in Chapter 2, SA refocused images can be calculated to be focused at specified z depths in the scene. They can in fact be calculated to be focused on arbitrary planes in the scene[1]. In order to achieve this, each point is back projected to lie on the specified plane. However, in this study, the focal plane is always maintained perpendicular to the z axis while calculating refocused images. This simplifies the mathematics involved in back projecting the points and also in locating points in

[1]SA refocused images can in theory be even calculated for curved surfaces in space such that objects lying on such a surface in space appear to be in focus in refocused images.

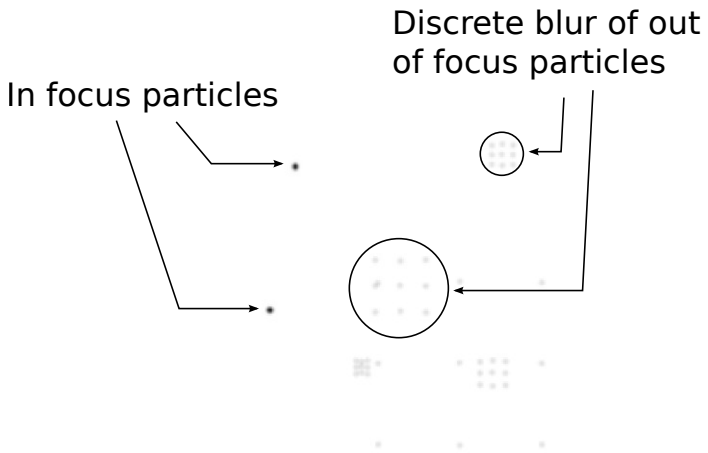

Figure 3-1: An example of the discrete blur that occurs in SA refocused images. *Note: this image has been inverted to improve visibility.*

space.

Since SA refocusing is achieved by combining images from discrete cameras and not from a real large aperture lens, objects in the refocused image that do not lie on the focal plane have a "discrete blur" (as shown in Fig. 3-1). Note how the shape of the blur or the point spread function is the same as the 2D projection of camera locations on the xy plane (Figure 1-2).

Since each image is either divided by N or raised to the power 1/N, the discrete blur of every out of focus particle has an intensity much lower than the intensity of the particle in the original image and thus can be removed by thresholding an image to an appropriate extent such that the intensity of every pixel below a certain intensity level T is set to zero. However, when a multiplicative method is used to refocus, the blur is automatically removed because the pixels representing the blur are multiplied by zero intensity pixels in another image. This thresholded image then only has particles visible that are, or are almost, in focus at the given z depth and thus can then be used to search for particles using algorithms used for 2D PTV. Sometimes discrete blurs of two (or more) different particles can align in a refocused image such that pixels are added (or multiplied) to form the SA equivalent of, as referred to in tomographic PIV, a "ghost particle" [11]. The intensity of this ghost particle is rarely as much as that of an actual particle because for that to happen a significant number

of blur patterns would have to align. Note that such an aligment would only occur for certain specific 3D configurations of particles and such a configuration would change over time because the particles would move to different locations. As a result, ghost particles would only be visible as flashes at random time instants and can thus be rejected.

3.1.2 Preprocessing Steps

Given that simulated images have a perfectly black background and have very similar looking (in both shape and intensity) particles, they only need to be processed after refocusing to remove the discrete blur of out of focus particles. However, real images contain noise and particles of varying shape and intensity and need to be preprocessed so that refocused images only contain in focus particles the particle detection scheme can efficiently locate them. It was found that a combination of adaptive intensity normalization, gaussian blurring and thresholding was efficient at eliminating noise and accentuating intensity peaks that likely represent real particles. Adaptive intensity normalization is performed by applying local intensity normalization in small windows over an entire image.

Figure 3-2 shows how a real image changes as preprocessing steps are applied. An initial thresholding step removes noise and particles that have really low intensity values. Adaptive intensity normalization then scales different intensity peaks such that they have similar intensity levels as shown. A gaussian blur is applied in order to increase the size of individual particles in the image so that back projected rays from pixels representing particles intersect despite the presence of small calibration errors. Since the blur step reduces the intensity of peaks it is followed by an additional adaptive intensity normalization step. The last thresholding step can be performed if cleaner refocused images are desired. It must be noted that this thresholding step removes some intensity peaks thereby reducing the number of particles detected in the reconstructed volume.

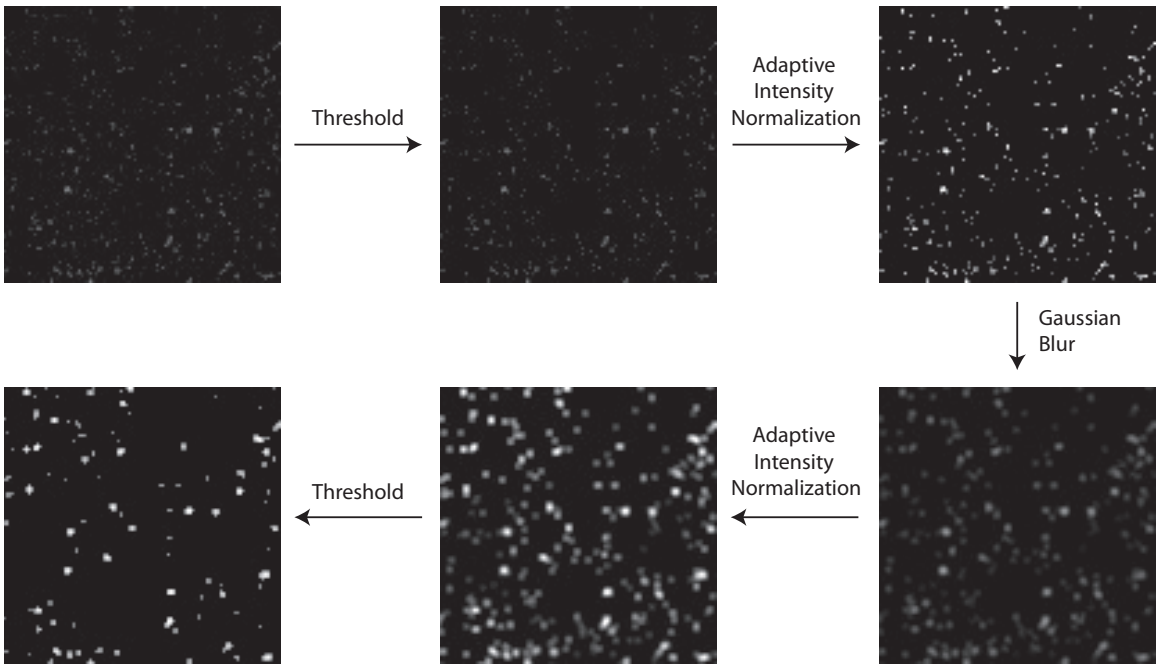

Figure 3-2: Typical preprocessing steps used on experimental data to accentuate particles and remove noise.

3.2 2D Particle Detection

Several particle detection techniques have been developed for use in 2D PTV which look for particles in images based on the fact that particles in grayscale PIV data look like a group of gray or white pixels. The dynamic threshold binarization technique proposed by Ohmi et al [23] has been shown to be very effective in searching for particles that have different intensity levels. A similar technique is used to detect particles in the images but without using any thresholding.

The algorithm implemented only looks for local intensity peaks in the image and then converges to the local maximum of each peak. Different edges of the same particle converge to the same peak and this is checked for in order to remove duplicate particles. An assumption about the minimum size of each particle is made to further get rid of apparent particles that might be noise or ghosts. An intensity weighted average scheme is then used to further refine the particle location to a sub pixel level.

3.3 3D Location Inference

As one changes the focus through the investigation volume using SA refocusing, each particle goes in and out of focus as shown in Fig. 3-4. 2D particle detection, as outlined in Section 3.2, is performed on the images refocused at different focal depths, distance dz apart covering the entire volume of interest. dz has a lower bound dz_{min} below which intensity values of pixels representing a particle are the same in adjacent images in a focal stack. This lower bound depends on the baseline spacing of the camera array as defined by Belden [8] which is a function of dx, dy, and D as shown in Figure 1-2). Figure 3-3 shows a plot of similarity between an image I_{ref} refocused at depth z_{ref} and an image I_{dz} refocused at depth dz away from z_{ref} using different thresholding levels. Similarity between images here is defined as:

$$Similarity(I_{ref}, I_{dz}) = \frac{sum(I_{ref} \circ I_{dz})}{sum(I_{ref} \circ I_{ref}) sum(I_{dz} \circ I_{dz})} \tag{3.1}$$

where $sum(A)$ is the sum of all elements in matrix A and $A \circ B$ is the Hadamard product of matrices A and B. Results show that the images can be refocused a very small dz (as low as 0.01 mm) apart and still have a detectable difference. This dz is actually smaller than dz_{min} but adjacent images have a detectable difference because they contain multiple particles and a few particles do change in intensity. This is of significance because particle localization accuracy in the z direction continues to improve even when dz decreases belwo dz_{min}. It must be noted that resolution in z decreases at thresholding level is increased.

After identifying particles in each refocused image, one can obtain the x, y and z coordinates of particles where the x and y coordinates are derived from the 2D location of the particle in an image and the z coordinate is the depth at which the focus of the image lies in which the particle has been detected. As a result, one can obtain a cloud of points where tight point clusters represent actual particles in space as shown in Figure 3-5. Points in these clusters can be grouped together and then used to calculate the locations of particles in space. In each such cluster, points differ

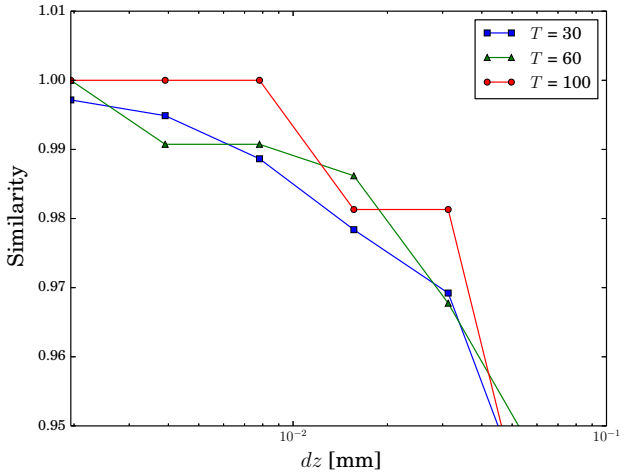

Figure 3-3: Similarity (defined in Equation 3.1 between images I_{red} and I_{dz} for different thresholding levels T

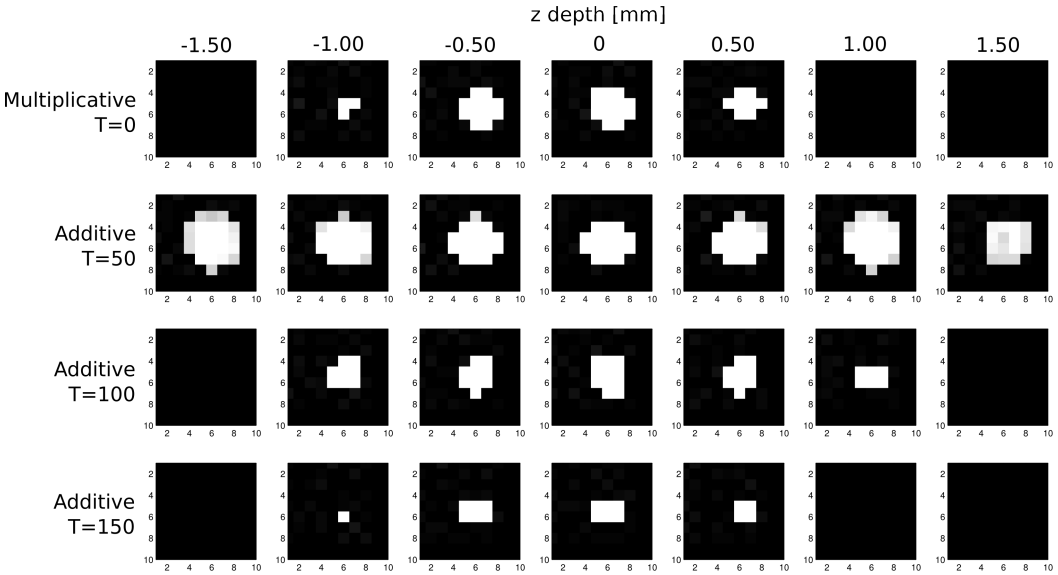

Figure 3-4: Particle going in and out of focus in a synthetic image as the focal depth is changed shown for different thresholding levels. T is the intensity level below which pixel intensity is set to zero.

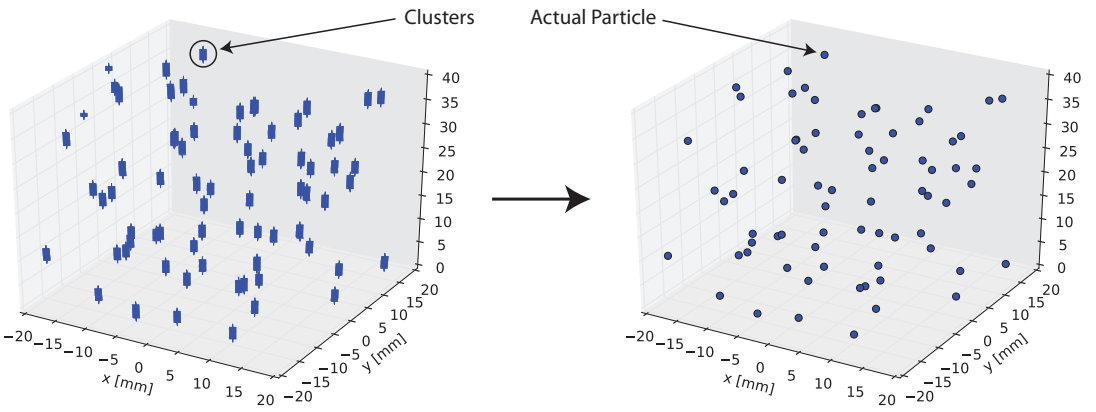

Figure 3-5: Collapsing clusters of points from 2D particle detection to actual particle locations

very slightly in x and y coordinates and in average intensity over z. It is observed that the x and y coordinates do not change much over z in a cluster and thus they are averaged in order to calculate the x and y coordinates for the particle.

Each particle is generally visible over a range in the z direction which is considerably larger than its actual physical z (as evident in Figure 3-4). Multiple methods can be used to estimate the z coordinate of clusters. 3 methods that were studied are named and defined here for sake of clarity:

1. z_{mean} method: z coordinate of particle is the mean z coordinates of detected points in a cluster.

2. Fit_{quad} method: A quadratic curve is fit to the average intensity distribution vs. z in each cluster and location of its peak is the z coordinate of particle.

3. Fit_{gauss} method: A gaussian curve is fit to the average intensity distribution vs. z in each cluster and location of its peak is the z coordinate of particle.

The average intensity of points in a cluster varies in z showing a maximum. Figure 3-6 shows, for all particles from a 100 particle test case, the variation of average detected point intensity with its z depth centered around the average z of each cluster. The trend shown here can be estimated using a quadratic or gaussian curve and consequently its z coordinate can be calculating by finding the peak of this curve. Accuracy of these methods is addressed in Section 3.4.

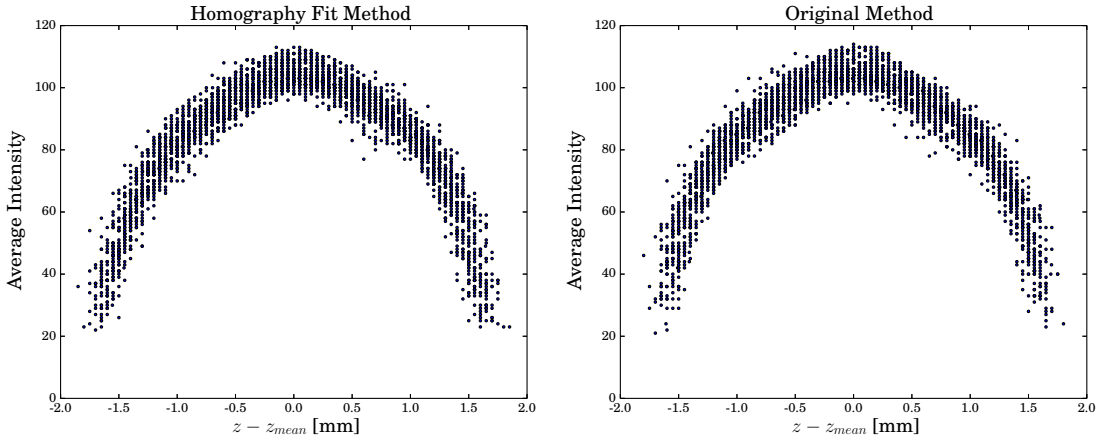

Figure 3-6: Variation of average intensity of detected point vs. z depth centered around the average z of each cluster for a test case of 100 points

Since any particle is visible over a certain z range, multiple particles having nearly identical x and y coordinates lying very close to each other in z will be interpreted as one particle. This situation however, is unlikely to occur in a seeded tank that is well mixed and will mostly only occur at a single time instant in a flow field.

3.4 Particle Localization Accuracy

The particle detection scheme outlined in Section 3.2 looks for local intensity peaks in images and thus point in discrete blurs of out of focus particles are also confused for particles. These can be removed by thresholding the image to a certain extent. Too much thresholding however begins to remove some particles that are in focus reducing the z range over which a particle is visible in refocused images as shown in Figure 3-4. As a result images must be thresholded to the right level in order to maximize particle detection. Figure 3-7 shows how the number of particles detected in a synthetic volume changes with the thresholding level T. It can be seen that if thresholding level is too low then too many particles are detected. The number of correct particles detected is maximum around a certain thresholding level. More particles can be detected even for high thresholding levels if the decrease in visibility range in the z direction is accounted for.

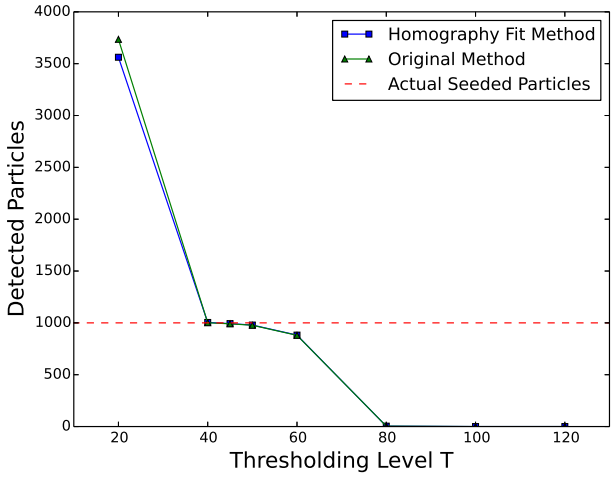

Figure 3-7: Number of particles detected vs. thresholding level T. The dotted line indicates the number of particles actually seeded in the synthetic volume which is 1000 in this case.

To study the accuracy of particle localization in space, localization error d_i^j and an average localization error ϵ_i in direction i are defined as:

$$d_i^j = \hat{x}_i^j - x_i^j \tag{3.2}$$

$$\epsilon_i = \frac{1}{N}\sum_{j}^{N} |d_i^j| \tag{3.3}$$

where $\hat{x}_i^j$ is the i (which can be x, y or z) coordinate of the j^{th} detected particle, x_i^j is the i coordinate of the actual j^{th} seeded particle and N is the number of particles. For a case of 100 particles seeded in a synthetic volume, both refocusing methods were used to locate particles and these locations were compared with actual seeding locations. Figures 3-8 and 3-9 show plots of d_i^j for each direction using the HF method and the original refocusing method respectively and Table 3.1 summarizes the average localization errors. It is observed that d_x^j and d_y^j show a trend with respect to x and y respectively which can be explained on the basis of calibration errors which can lead to small amounts of rotation, shift or scaling in refocused images as outlined in Section 3.4.1. This will only shift detected particles compared to seeded particles but

Table 3.1: Summary of average localization errors for both refocusing methods

	HF Method	Original Method
ϵ_x	0.0523	0.0529
ϵ_y	0.0992	0.0995
ϵ_z	0.3267	0.0397

the relative location of particles will remain the same and hence any flow structures will not be affected.

The error in z direction d_z^j however does not seem to follow a trend with z. However, when the HF method is uses, d_z^j shows a trend with respect to x. This is likely to do a pixel level error in mapping of the image using the calculated homography matrix. Further exploration of the underlying cause of this trend might help increase the particle localization accuracy of the HF method. It must be noted that ϵ_z for the original refocusing method is found to be smaller than that for the HF method. Section 3.4.1 shows how this difference in error for both methods becomes much smaller for experimental data due to calibration errors.

3.4.1 Calibration Error

The calibration process, as outlined in Section 2.1, simultaneously optimizes the location of 3D world points (corresponding to corners on used chessboard pattern for used images) and camera parameters such that the reprojection error of each point is minimized. In order to allow validation of the particle localization process, the world coordinate system in the calibrated results is aligned to the physical grid used such that the grid in a specific image lies on the center of the xy plane. Calibration errors, as a result, can be of 2 kinds:

1. Error in alignment of calibration coordinate system to the coordinate system in the simulation. This includes scaling, rotation and translation errors.

2. Error in the relative pose of the cameras in the array with respect to each other and the origin.

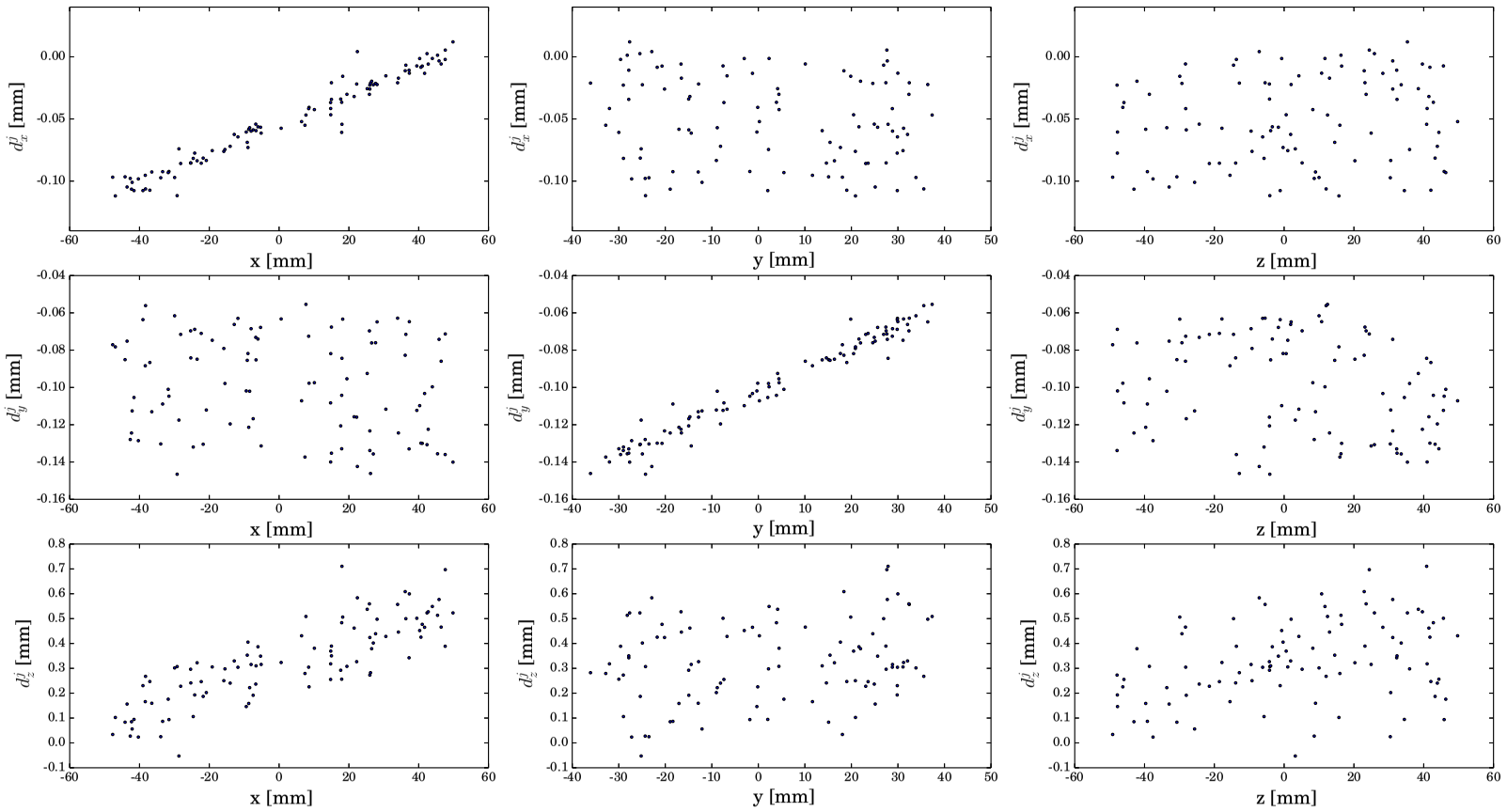

Figure 3-8: Localization errors d_i^j for detected particles in each direction using the Homography Fit method.

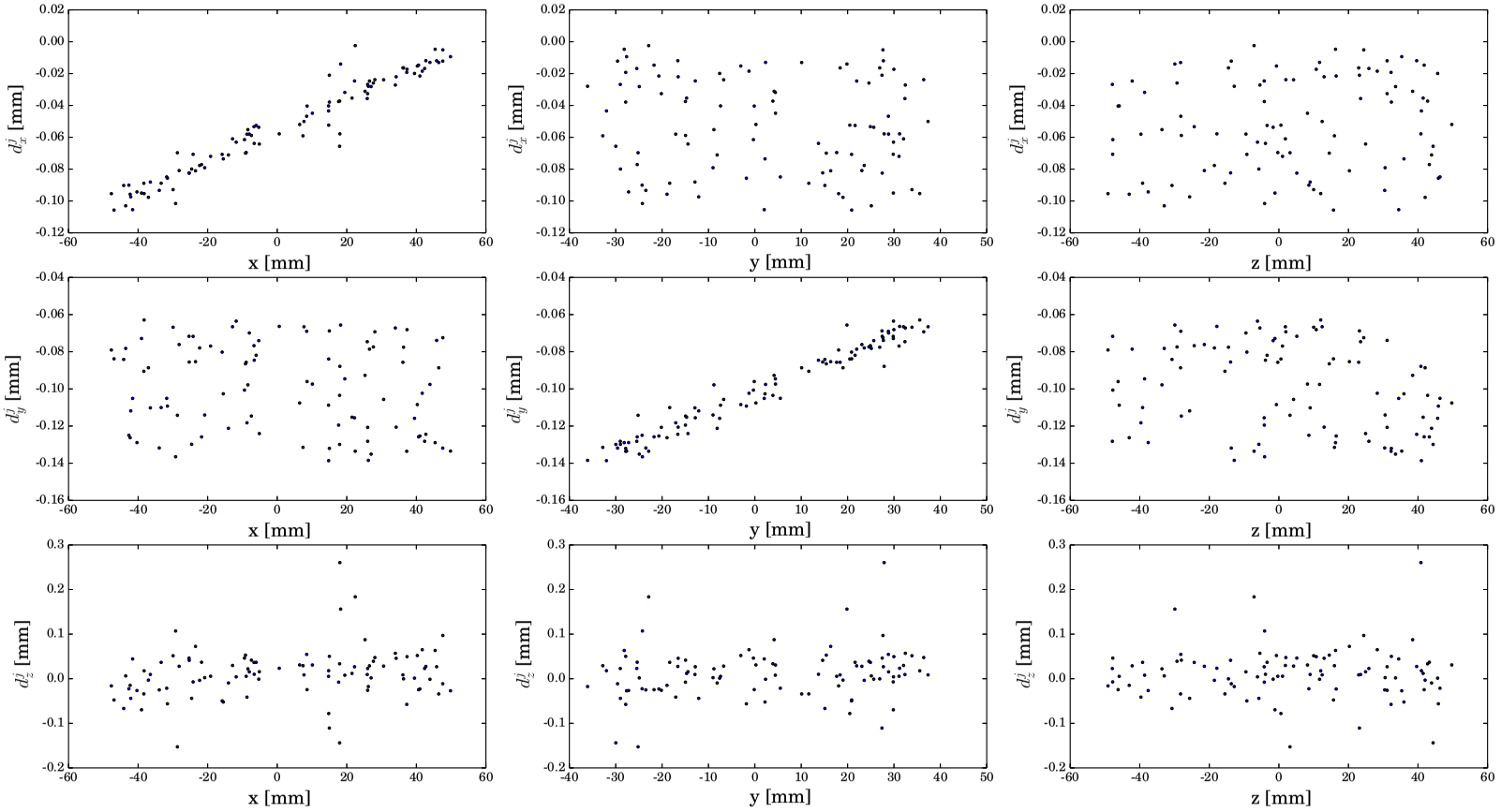

Figure 3-9: Localization errors d_i^j for detected particles in each direction using the original refocusing method.

Note that errors of the first kind will affect calculated values of d_i^j for each point but will not affect the relative location of particles to each other. This is why any flow features will not be affected.

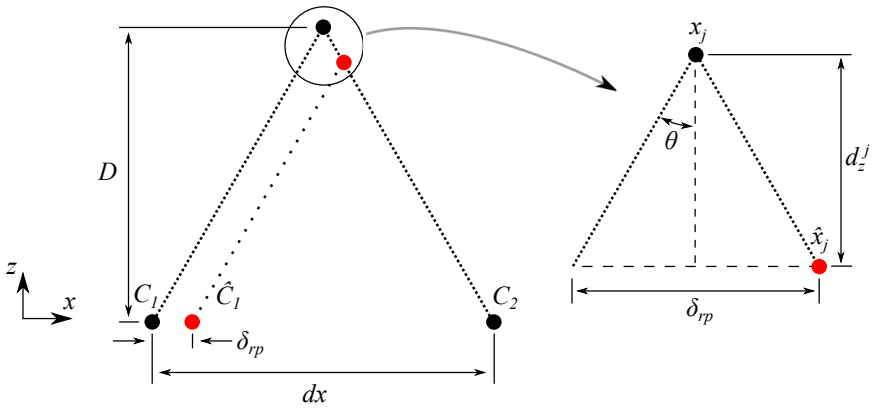

Figure 3-10: Effect of error δ_{rp} in camera location on error d_z^j in the z location of j^{th} particle. dx and D are the same as in Figure 1-2 and x_j and $\hat{x}_j$ are the actual and calculated locations of the particle respectively.

However, errors of the second kind will affect the relative location of particles. If the cameras are misaligned relative to each other such that back projected rays do not intersect in space then some particles will not be visible in the reconstructed volume. However, if the cameras are misaligned in such a way that the back projected rays do intersect but at a point other than the true location of the particle then the error can be quantified based on the maximum reprojection error in the calibration process. Figure 3-10 shows a simple case involving 2 cameras in which the error in camera location is such that the calculated camera location $\hat{C}_1$ of camera 1, the actual location C_1 of camera 1, the actual location C_2 of camera 2 and the point of intersection of back projected rays all lie in the same plane. If in such a case error in location of camera 1 is δ_{rp} (corresponding to the maximum reprojection error due to a shift in camera location), the resulting error d_z^j in the z coordinate of the j^{th} particle can be calculated as:

$$\frac{\delta_{rp}}{2d_z^j} = \frac{dx}{2D} \tag{3.4}$$

$$d_z^j = \frac{D}{dx}\delta_{rp} \tag{3.5}$$

The ratio D/dx typically has a value between 2 and 3 and δ_{rp} for an acceptable calibration is about 0.04 mm (about 0.4 pixels). Thus solely due to calibration error, d_z^j can be about $\pm$ 0.1 mm which is in the same order of magnitude as ϵ_z for the HF method.

3.4.2 Error in Particle z Coordinates

For synthetic data, accuracy of estimation of particle z coordinates is found to be influenced by the method used to calculate the z coordinate of each cluster and by which method is used to refocus images. Figure 3-11 shows how ϵ_z varies with dz used to reconstruct the volume for different z estimation methods. As mentioned earlier, ϵ_z is larger when the HF method is used to refocus the images. A compromise is thus made in z error for the significant increase in computation speed that the HF method achieves. It is also evident that since a smaller dz (even smaller than dz_{min}) provides a higher resolution, it also provides a better estimate of particle z coordinates. However, it must be pointed out here that the effect of calibration error on the error in particle z coordinates, as outlined in Section 3.4.1, can be large enough to render the HF method comparable to the original refocusing method in terms of accuracy.

When the original refocusing method is used, ϵ_z increases with dz regardless of the z estimation method and it increases much more rapidly for the z_{mean} method. dz does not seem to affect accuracy of the HF method.

Both fitting methods are more computationally intensive than the z_{mean} method but this extra computation time can be traded for the increase in speed achieved when a larger dz is used. Reconstructing a volume will take $1/5^{th}$ the time if a dz

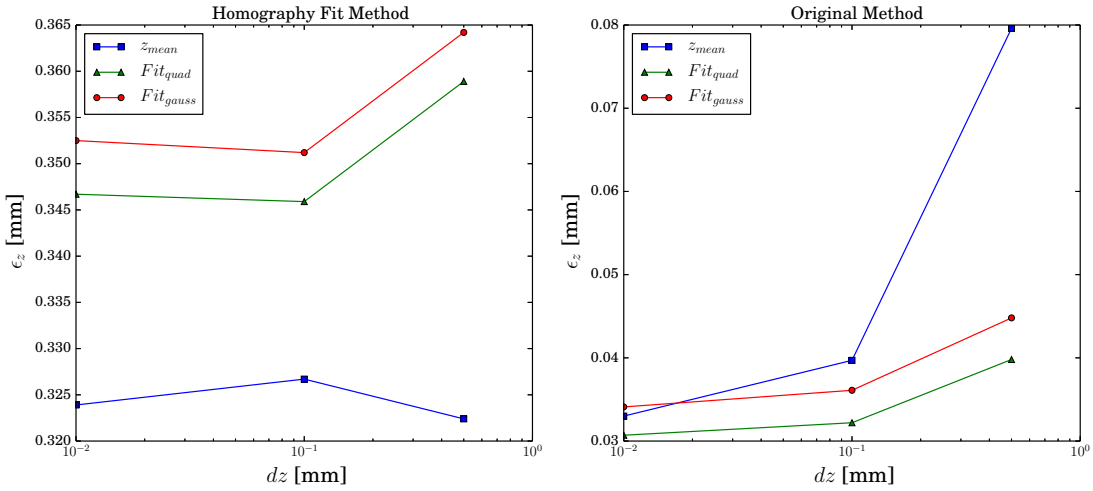

Figure 3-11: Varation of ϵ_z with dz used to reconstruct volume shown for different z estimation methods

of 0.5 mm is used instead of 0.1 mm. As a result, based on results shown in Table 2.1, the original refocusing method can be used to recontruct the same volume used for benchmarking in about 10 minutes using a dz of 0.5 mm (Desktop + GPU) while still achieving a much lower ϵ_z (ϵ_x and ϵ_y show negligible change with dz and are comparable for both refocusing methods). The time taken thus is still much larger than that compared to the HF method but this time trade off for particle localization accuracy can be easier to justify.

It must be mentioned here that all particles in experimental data do not necessarily follow an intensity profile as shown in Figure 3-6 and errors due to calibration and the actual intensity profile can amplify ϵ_z for both refocusing methods and likely render both methods approximately as accurate as each other. As a result the HF method becomes the method of choice due to the drastic increase in computation speed that it offers.

THIS PAGE INTENTIONALLY LEFT BLANK

Chapter 4

Particle Tracking

Over the last few decades, several techniques have been developed to track particles, both in two and three dimensions. Their performance varies depending on the experimental setup used and the kind of flow being analyzed. Hassan and Canaan [15] used a 4 frame tracking method to analyze a bubbly flow, in which a track is selected based on the minimum variance of length and angle of travel between consecutive frames out of all paths possible. Baek and Lee [4] presented a new 2 frame tracking technique based on match probability. This method is based on the estimation of match and no match probabilities for each particle via iteration using local flow similarity as a weighting factor to increase match probability. Ohmi and Lam [22] presented a new tracking method, which they called the relaxation method, which was later implemented in detail by Ohmi and Li [23]. This method is based on the original method used by Barnard and Thompson [5] for analysis of motion of humans and automobiles recorded in a scene. Mathematically, the relaxation method is essentially the same method as used by Baek and Lee but the implementation by Ohmi et al is slightly more computationally expensive.

Other authors (Labonte [19]) have implemented neural network based techniques which are mostly based on the self organizing map (SOM) proposed by Kohonen [18]. Pereira et al [25] compared the relaxation, neural network, and basic nearest neighbor methods and found that the relaxation method performed best followed by the neural network method. Jia et al [16] suggested an improved relaxation method in which

neighbor sets are built based not on a neighborhood radius but on results of a Delaunay tessellation. This method was found to perform as well as the relaxation method but was more robust for different particle densities. Ruhnau [26] had presented a variational approach for conducting PTV which was found to perform better than the relaxation method by Pereira et al but was not analyzed in detail. In general, PTV becomes infeasible beyond a certain particle seeding density and the only option left is PIV. However, for low seeding densities, PTV can provide good results if the appropriate tracking method is used. For 3D cases with acceptable seeding density, PTV is found to be the method of choice [25].

4.1 The Relaxation Method

In this study, the relaxation method was used to track the particles. Pereira and Jia ([25], [16]) discuss this technique in extensive detail. The relaxation method is an iterative method which uses constraints derived from known aspects about the flow such as flow similarity, velocity, etc. The first step in implementing this method is to build reference and candidate sets S_r and S_c respectively such that:

$$S_r = \{x_k : |x_i - x_k| < R_n\} \tag{4.1}$$

$$S_c = \{y_j : |x_i - y_j| < R_s\} \tag{4.2}$$

where x_i is the location of a particle in the first frame and y_i is the location of a particle in the second frame, R_n is the neighborhood threshold and R_s is the maximum movement threshold. Figure 4-1 shows a schematic of how these sets are built. The next step is to find, for each particle x_i in S_r, the most probable matching particle in S_c. This is achieved by defining a matching probability P_{ij} between each particle in S_r and particle in S_c. In addition, for particle in S_r, a probability P_i that particle has no match in S_c is defined. These probabilities must satisfy the following condition:

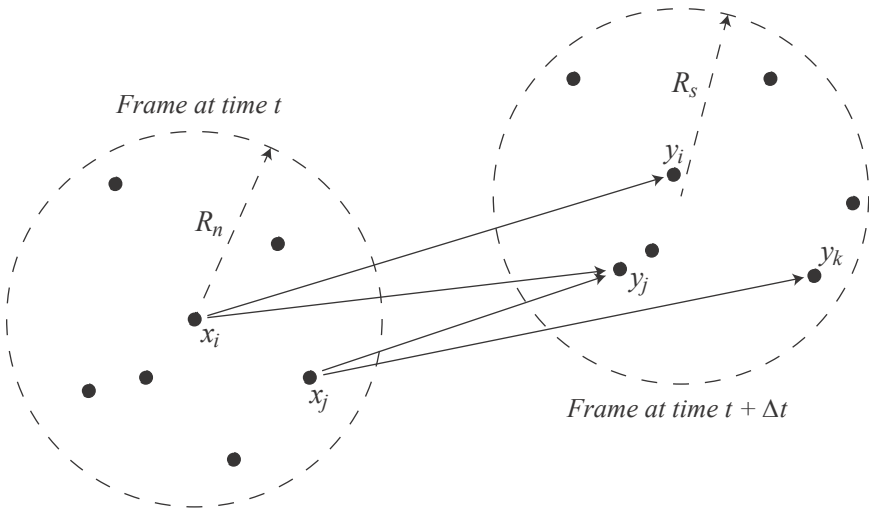

Figure 4-1: Schematic showing how reference and candidate sets are built for use with the relaxation tracking method

$$\sum_{i \in S_r, j \in S_c} P_{ij} + P_i = 1 \tag{4.3}$$

and are initialized as:

$$P_{ij}^{(0)} = P_i^{(0)} = 1/(M_i + 1) \tag{4.4}$$

where M_i is the number of particles in S_c and the superscripts in Equation 4.4 indicate the iteration number. These probabilities are then iteratively updated as:

$$\tilde{P_{ij}^{(n)}} = P_{ij}^{(n-1)} \left(A + B \sum_{k,l \in \Theta} P_{kl}^{n-1} \right) \tag{4.5}$$

$$\Theta = \{(k,l) : |d_{ij} - d_{kl}| < E + F|d_{ij}|\} \tag{4.6}$$

where A and B are weighting constants ($A = 0.3$ and $B = 3.0$ [5], [23]), $d_{ij} = x_i - y_j$ and $d_{kl} = x_k - y_l$. E and F are constants that determine the relaxation area that enforces a quasi rigidity constraint ($E = 1.0$ and $F = 0.05$ [23]). The last step of each

loop is to normalize all probablities such that they satisfy Eqn. 4.3:

$$P_{ij}^{(n)} = \frac{\tilde{P_{ij}^{(n)}}}{\sum_j \tilde{P_{ij}^{(n)}} + \tilde{P_i^{(n)}}} \tag{4.7}$$

$$P_i^{(n)} = \frac{\tilde{P_i^{(n)}}}{\sum_j \tilde{P_{ij}^{(n)}} + \tilde{P_i^{(n)}}} \tag{4.8}$$

The match probabilies generally converge in about 10 to 20 iterations. For denser particle distributions, the number of iterations required for convergence are more. Since this tracking method works on only two consecutive frames at a time, particles coming into the volume and leaving the volume can be tracked for only the duration over which they are visible. However, for experimental data, it is beneficial to filter out paths that are smaller than a certain number of frames as they might represent incorrect links.

Performance of the tracking method is studied based on a recovery ratio η_r, defined by Pereira [25] as:

$$\eta_r = \frac{M_{cl}}{N_{cl}} \tag{4.9}$$

where M_{cl} is the number of correct links found by the tracking algorithm and N_{cl} is the total number of correct links. Test cases were generated seeded with N_p particles in a volume of size 150 mm in all directions and were propagated according to a vortex ring of different ciculation strenghs Γ[1] over a duration of 1 second at 30 Hz. Figure 4-2 shows how η_r, for tracking between frames 15 and 16, varies with the neighborhood and maximum movement thresholds R_n and R_s (which in this case are considered to be equal since investigation reveals that η_r is maximum when R_n and R_s are about the same value). Table 4.1 summarizes η_r for different cases shown in Figure 4-2 with tracking parameter ϕ, again defined by Pereira [25] as:

[1]Note that the maximum distance moved by a particle in the volume depends on the value of Γ

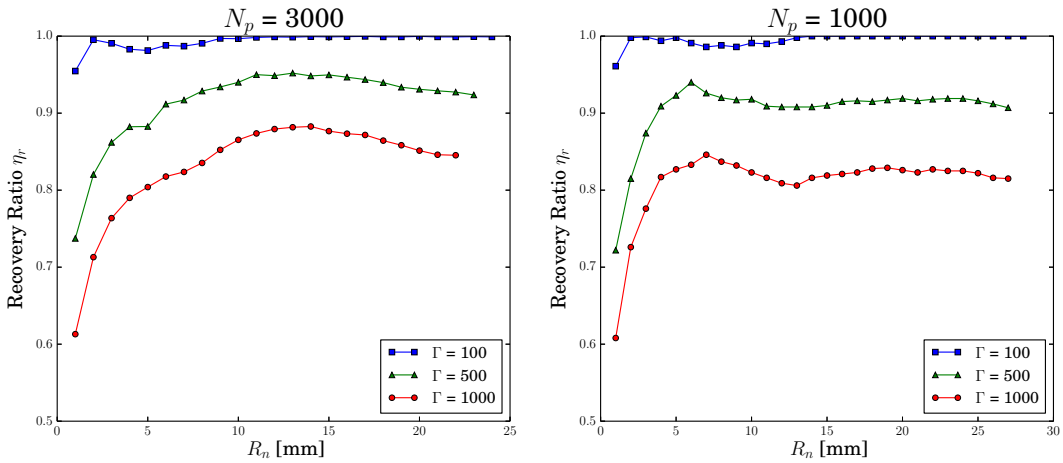

Figure 4-2: Variation of tracking algorithm performance with neighborhood threshold size R_n. N_p is the number of seeded particles.

Table 4.1: Summary of peak tracking algorithm performance for different cases

Case #	N_p	ϕ	Peak η_r	R_n [mm]
1	1000	7.597	1.000	14
2	1000	1.558	0.926	7
3	1000	0.833	0.846	7
4	3000	5.267	0.999	7
5	3000	1.081	0.952	13
6	3000	0.578	0.883	14

$$\phi = \frac{d_0}{|x|_{max}} \tag{4.10}$$

where d_0 is the mean distance between particles and $|x|_{max}$ is the maximum distance moved by a particle in the investigation volume.

It can be seen in Figure 4-2 that the algorithm performs really well for low values of Γ which imply low values of $|x|_{max}$ and consequently high values of ϕ. As expected, performance becomes worse as ϕ becomes smaller. Note how optimal performance for different cases is achieved at different values of R_n. It must also be mentioned that the constants E and F, since they define the relaxation area, are likely to affect

the tracking performance too. Due to the difference in velocity gradients in different flows, the optimal relaxation area for different flows is different. If R_n, E, and F are varied, it is found that higher values of peak η_r can be achieved. For Case 2 (Table 4.1), a peak η_r of 0.941 can be achieved if $R_n = 19$, $F = 2.9$ and $E = 0.175$ (R_s was same as R_n). An in depth study of optimal values of R_n, R_s, E and F for different values of ϕ was not conducted.

Once particles have been tracked over several consecutive frames, their velocities can be used to calculate a regularized velocity field in the investigation volume by interpolating to a grid. Figure 4-3 shows a plot of particle trajectories (longer than 5 frames over all 30 frames) for Case 4 (Table 4.1). Figure 4-4 shows interpolated velocity and vorticity magnitude fields at the xz and yz planes between frames 15 and 16.

Other tracking methods, especially the variational method [26] studied by Ruhnau, can potentially be more accurate for flows with smaller values of ϕ, particularly for vortex flows. Studying the performance of different tracking algorithms however, is outside the scope of this thesis.

4.2 Experimental Validation

4.2.1 Experimental Setup

In order to test the developed technique, an experimental setup was constructed using an array of nine high speed cameras (capable of recording at a maximum frame rate of 3200 Hz) looking at a 5 gallon water tank. A vortex piston made using a pneumatic piston operated by a pump was used to generate vortex rings in the tank moving in the z direction shown in Figure 4-5. The vortex piston had an outlet diameter of 0.5 inch and a stroke length of 1 inch was used. The speed of the piston was adjusted such that the generated vortex ring would move across the visible y extent over about 30 frames. Synchronized data was recorded using all cameras at 250 Hz for two cases:

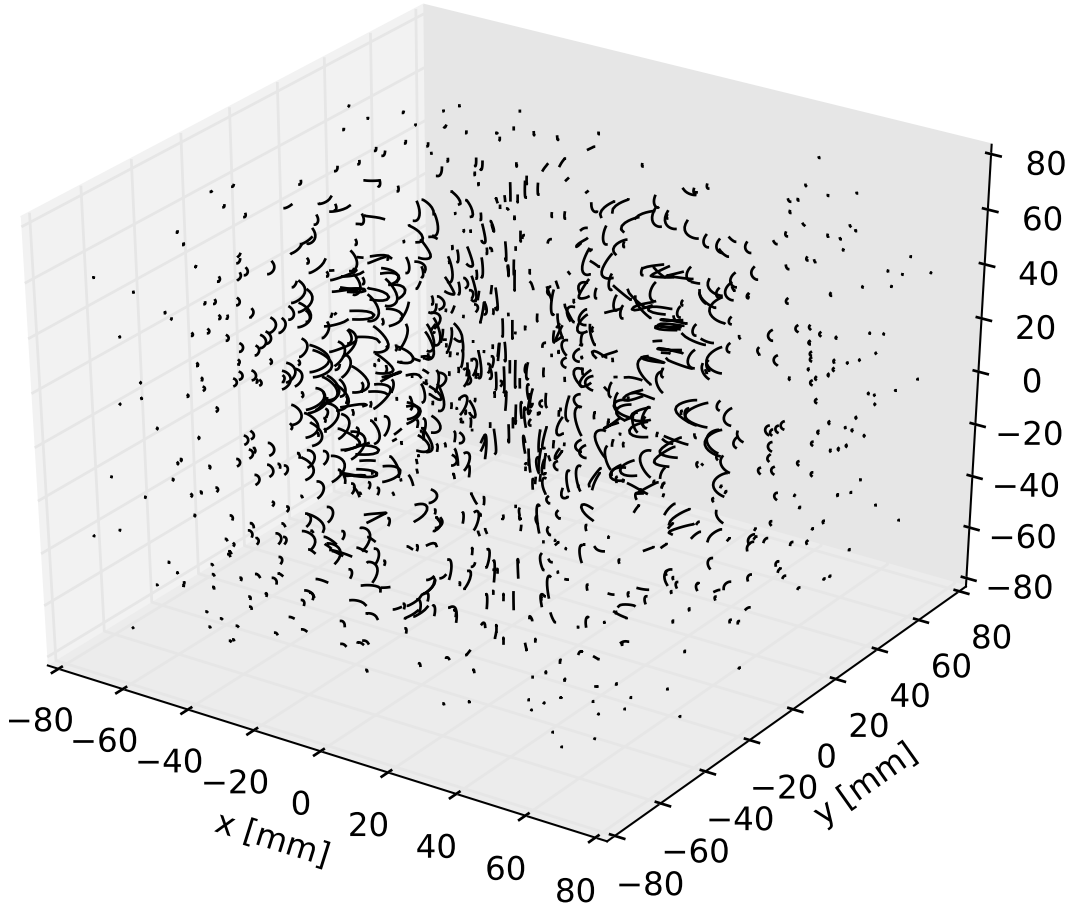

Figure 4-3: 2923 particle trajectories (out of actual 3000) across all 30 frames for Case 4 (Table 4.1). Trajectories visible for over 5 frames are shown. *Note: Only a third of all trajectories are shown to improve visibility.*

1. Case 1: Fluid in tank was water, seeded with 0.2 gms of particles

2. Case 2: Fluid was a shear thinning non Newtonian solution - 20 % by volume of Glycerol and 450 ppm xanthan gum, seeded with 0.1 gms of particles

For both cases, the tank was seeded with neutrally buoyant 50 micron polyamide seeding particles and was illuminated by a high speed near infrared volumetric laser such that the z extent of illuminated particles was about 40 mm. This limited z extent is because of a trade off between camera aperture size (large size to improve particle visibility) and focal depth. The z range within which SA refocusing can be performed must also be completely in focus in all cameras in the array. As one

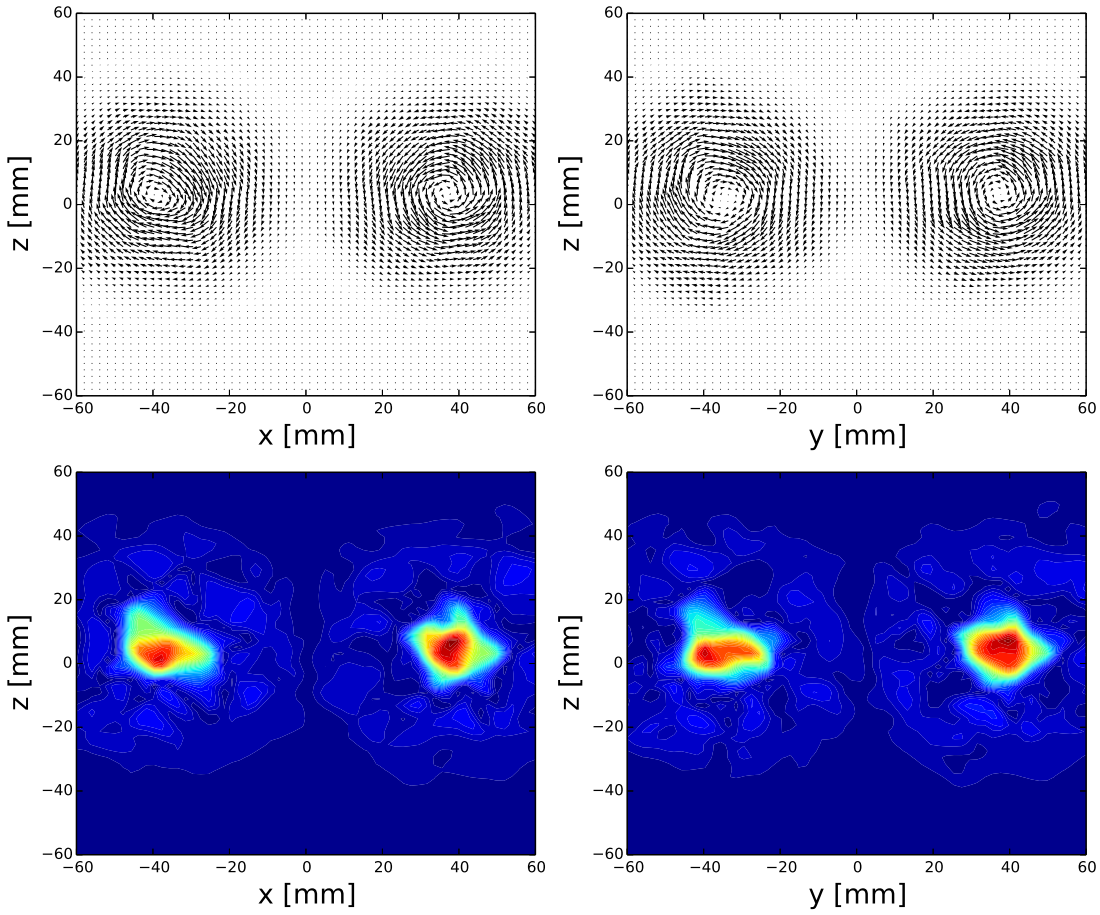

Figure 4-4: Interpolated velocity fields (without any smoothing) and vorticity magnitude fields (with smoothing) at xz and yz planes between frames 15 and 16 for Case 4.

increases recording frame rate, the pulse duration of illuminating laser decreases thus making particles less visible. The lens aperture size on the other cannot be increased beyond a point because then the focal depth becomes too small to be feasible. Figure 4-5 shows a picture of the experimental setup used.

4.2.2 Results

For both cases, the array was calibrated using a 5 x 5 chessboard pattern and the the mean reprojection error of all points after the calibration process was about 0.4 pixels. Recorded images were preprocessed using a combination of the steps

Figure 4-5: Experimental setup used to record data. Coordinate system set after calibration process is as shown in image.

mentioned in Section 3.1. Particles were detected in frames in which the vortex ring was visible and were tracked over 30 frames. Particle trajectores visible for over 5 or more frames were retained. Figure 4-6 shows a plot of 2700 particle trajectories across all 30 frames and Figure 4-7 shows interpolated velocity and vorticity magnitude fields at the xy and yz planes for one time instant in the processed sequence for case 1. Figure 4-8 shows a plot of 730 particle trajectories across all 30 frames and Figure 4-9 shows interpolated velocity and vorticity magnitude fields at the xy and yz planes for one time instant in the processed sequence for case 2.

From Figures 4-6 through 4-9, it is evident that results from experimental data validate the developed PTV technique. In addition, the results show that the developed technique can be used to obtain high spatial resolution PTV results if a high seeding density is used. The trajectories shown in Figure 4-6 are cropped to show only the region in which the vortex ring is visible and a total of about 4200 trajectories longer than 5 frames were resolved in the entire field of view. Cases with even higher seeding densities have not yet been tested. Results shown are based on volumes reconstructed using the HF refocusing method. Results based on volumes reconstructed using the original refocusing method were essentially identical to those shown.

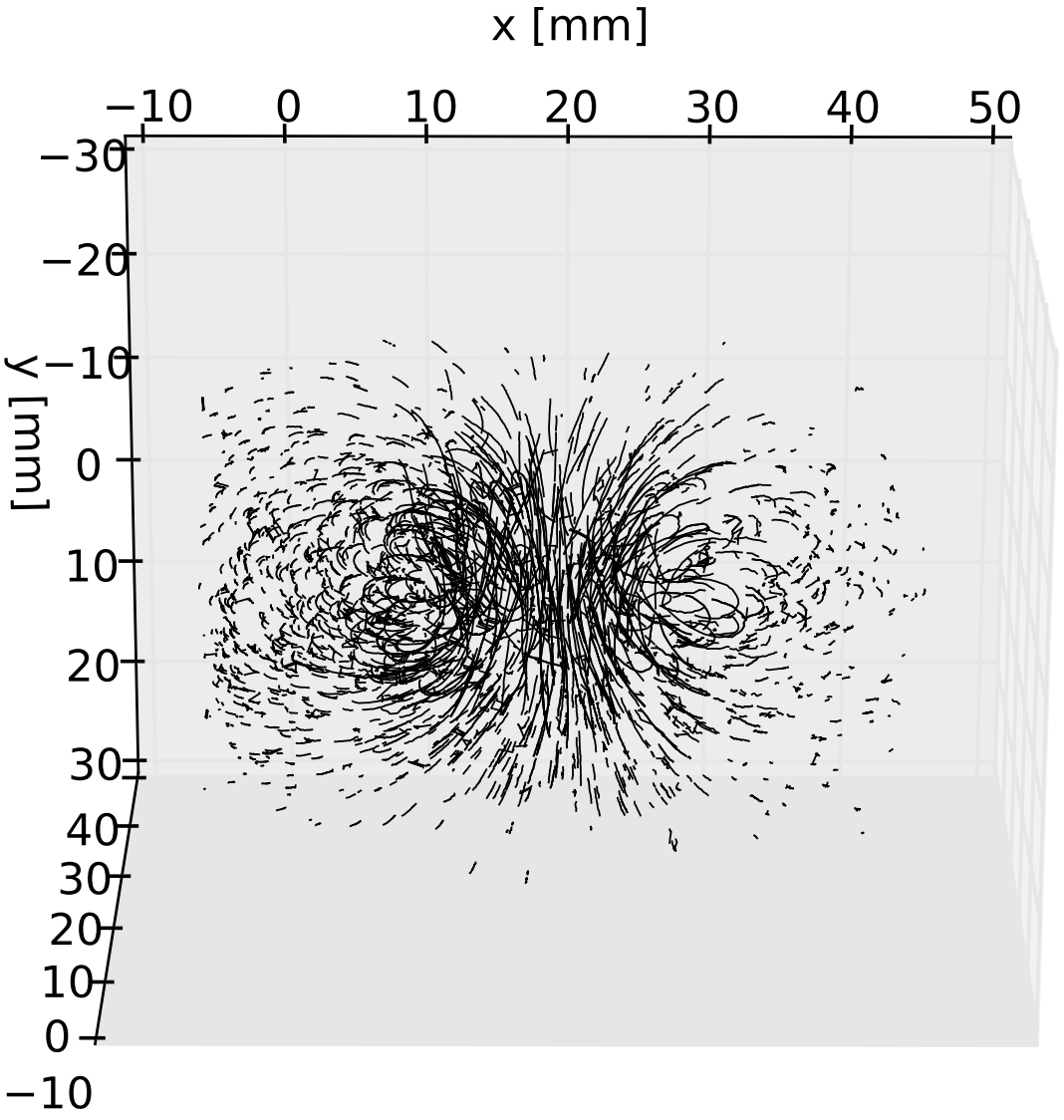

Figure 4-6: 2700 particle trajectories across all 30 frames shown for an case 1. Only trajectories visible for over 5 frames were retained and plotted.

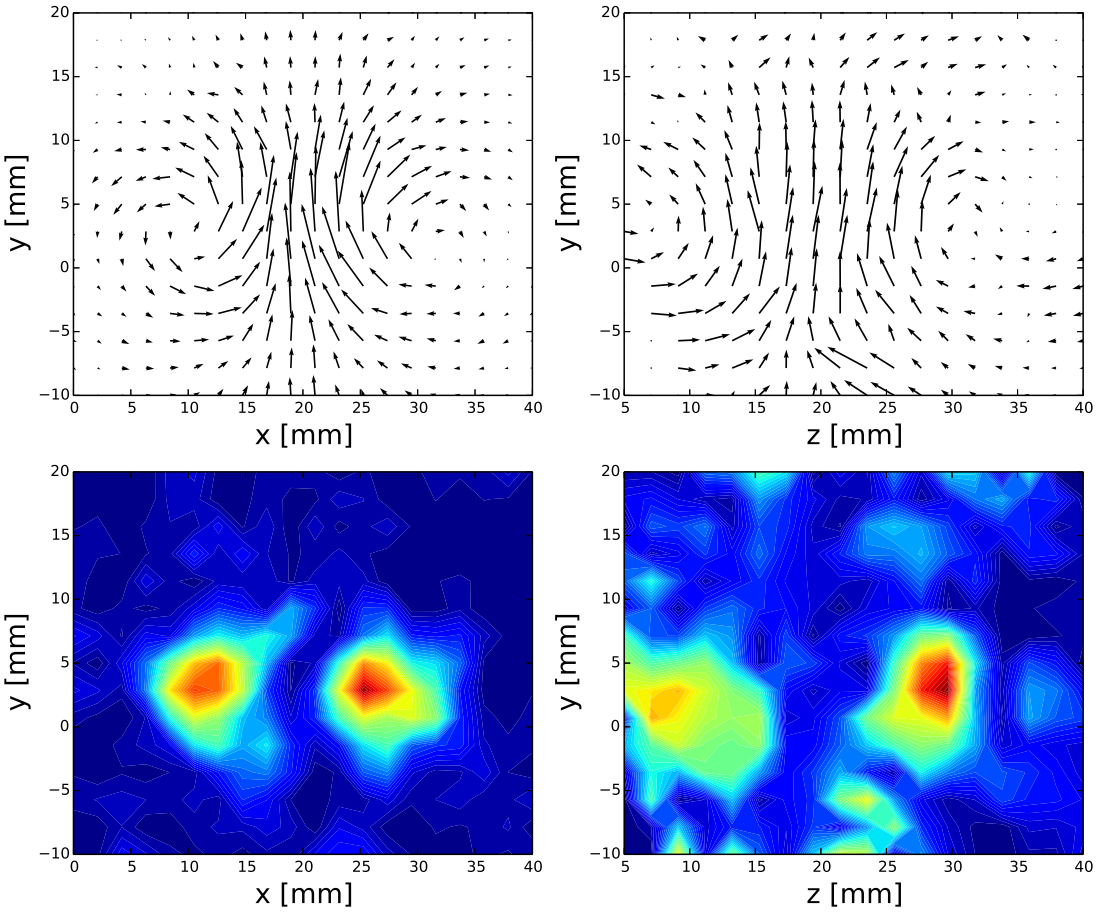

Figure 4-7: Interpolated velocity fields (without any smoothing) and vorticity magnitude fields (with smoothing) at xy and yz planes for one time instant in case 1.

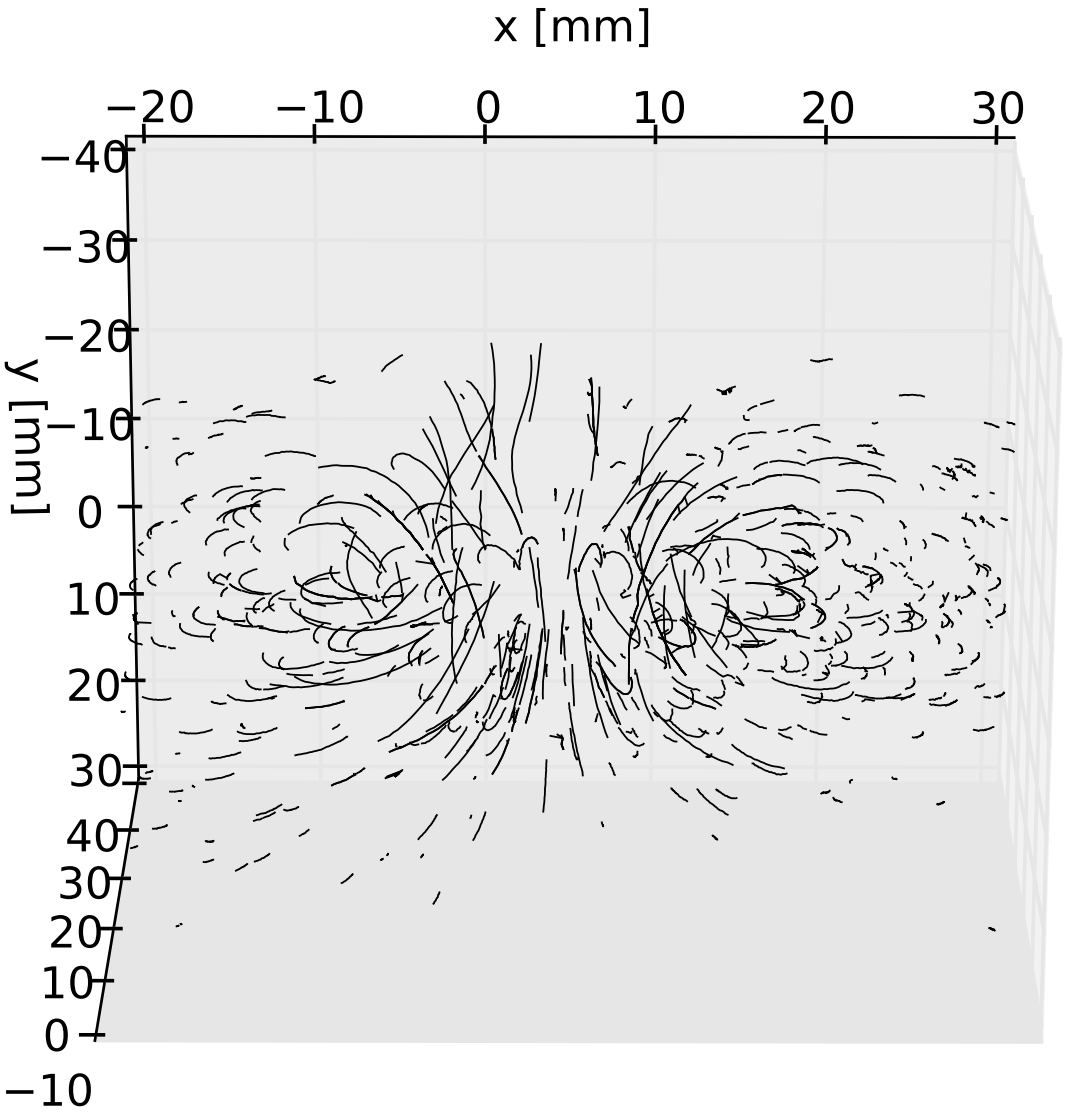

Figure 4-8: 730 particle trajectories across all 30 frames shown for an case 2. Only trajectories visible for over 5 frames were retained and plotted.

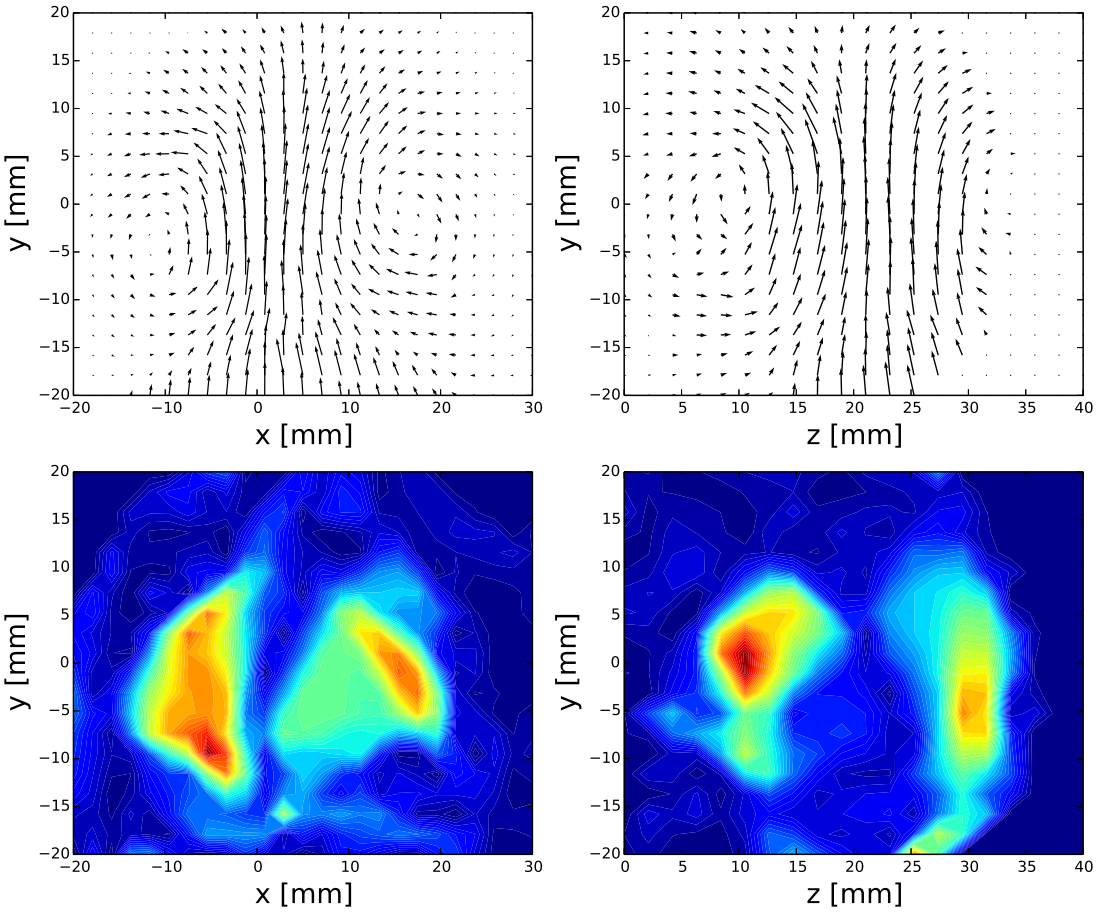

Figure 4-9: Interpolated velocity fields (without any smoothing) and vorticity magnitude fields (with smoothing) at xy and yz planes for one time instant in case 2.

Chapter 5

Conclusion and Outlook

This thesis shows that a 3D Particle Tracking Velocimetry (PTV) system based Synthetic Aperture (SA) imaging has been developed. SA imaging can thus be used to accurately calculate seeding particle locations in a volume which can be tracked over time using an appropriate tracking algorithm. In addition, the developed technique is able to achieve high spatial resolutions if a high particle seeding density is used.

Based on simulations, SA imaging can be used to reconstruct volumes having a z extent as large as the in-plane image field of view. As mentioned in Chapter 4, the size of this volume in z direction, for experimental data, is limited by the experimental hardware used. The volume size can be significantly increased by using a wider and a more powerful laser beam to illuminate the particles. There is a trade off between seeding density and size of investigation volume in the z direction. This is because the recorded images will rapidly start to saturate as the z extent of the volume increases, thus making it more and more difficult to localize particles. The speed of the flow being analyzed does not affect the performance of this technique and high speed flows only require higher speed cameras. In addition, using the HF refocusing method, SA imaging can reconstruct volumes in a much shorter time as compared to the time taken by the standard MART algorithm used in tomographiy. The advantges of SA PIV or PTV are summarized:

1. SA imaging has the potential to resolve a z extent larger than tomographic PIV

or PTV can.

2. SA imaging can reconstruct volumes in a time significantly shorter (details in Section 2.4) than the time taken by tomographic reconstruction if the HF method is used.

Work towards further development of this technique will include:

1. An in depth analysis of the accuracy of the HF refocusing method.

2. Estimation of the upper bound on seeding density that this technique can support.

3. Improvement in computation speed of the particle localization algorithm

One shortcoming of this technique is the cost since a larger number of cameras are used as compared to tomography. However the advantage in terms of computation speed can mitigate the significance of this shortcoming. Moreover, if the technique is further engineered to reduce the cost of the experimental setup it has the potential to become the method of choice to conduct both 3D PTV and PIV.

Bibliography

[1] JB Abbiss, TW Chubb, and ER Pike. Laser doppler anemometry. *Optics & Laser Technology*, 6(6):249–261, 1974.

[2] Ronald J Adrian. Twenty years of particle image velocimetry. *Experiments in Fluids*, 39(2):159–169, 2005.

[3] Callum Atkinson and Julio Soria. An efficient simultaneous reconstruction technique for tomographic particle image velocimetry. *Experiments in Fluids*, 47(4-5):553–568, 2009.

[4] S. J. Baek and S. J. Lee. A new two-frame particle tracking algorithm using match probability. *Experiments in Fluids*, 22:23–32, 1996.

[5] S T Barnard and W B Thompson. Disparity analysis of images. *IEEE transactions on pattern analysis and machine intelligence*, 2:333–340, 1980.

[6] Jesse Belden. *Synthetic Aperture Imaging for Three Dimensional Resolution of Fluid Flows*. PhD thesis, Massachusetts Institute of Technology, 2011.

[7] Jesse Belden, Sai Ravela, Tadd T. Truscott, and Alexandra H. Techet. Three-dimensional bubble field resolution using synthetic aperture imaging: application to a plunging jet. *Experiments in Fluids*, 53:839–861, 2012.

[8] Jesse Belden, Tadd T Truscott, Michael C Axiak, and Alexandra H Techet. Three-dimensional synthetic aperture particle image velocimetry. *Measurement Science and Technology*, 21(12):125403, 2010.

[9] Genevieve Comte-Bellot. Hot-wire anemometry. *Annual review of fluid mechanics*, 8(1):209–231, 1976.

[10] Deog Hee Doh, Gyeong Rae Cho, and Young Ho Kim. Development of a tomographic ptv. *Journal of mechanical science and technology*, 26(12):3811–3819, 2012.

[11] GE Elsinga, F Scarano, B Wieneke, and BW Van Oudheusden. Tomographic particle image velocimetry. *Experiments in Fluids*, 41(6):933–947, 2006.

[12] Richard Gilman Folsom. Review of the pitot tube. 1955.

[13] Rainer Hain, Christian J Kähler, and Dirk Michaelis. Tomographic and time resolved piv measurements on a finite cylinder mounted on a flat plate. *Experiments in fluids*, 45(4):715–724, 2008.

[14] R. I. Hartley and A. Zisserman. *Multiple View Geometry in Computer Vision*. Cambridge University Press, ISBN: 0521540518, second edition, 2004.

[15] YA Hassan and RE Canaan. Full-field bubbly flow velocity measurements using a multiframe particle tracking technique. *Experiments in fluids*, 12(1-2):49–60, 1991.

[16] P Jia, Y Wang, and Y Zhang. Improvement in the independence of relaxation method-based particle tracking velocimetry. *Measurement Science and Technology*, 24(5):055301, 2013.

[17] J Kitzhofer and C Brücker. Tomographic particle tracking velocimetry using telecentric imaging. *Experiments in fluids*, 49(6):1307–1324, 2010.

[18] Tuevo Kohonen. Self-organizing and associative memory. *Springer, Berlin*, 1989.

[19] Gilles Labonté. A new neural network for particle-tracking velocimetry. *Experiments in Fluids*, 26(4):340–346, 1999.

[20] Matteo Novara, Kees Joost Batenburg, and Fulvio Scarano. Motion tracking-enhanced mart for tomographic piv. *Measurement science and technology*, 21(3):035401, 2010.

[21] Matteo Novara and Fulvio Scarano. A particle-tracking approach for accurate material derivative measurements with tomographic piv. *Experiments in fluids*, 54(8):1–12, 2013.

[22] K Ohmi and Dao Hai Lam. New particle tracking piv using an improved relaxation method. In *CD Rom Proc. of 8th International Symposium on Flow Visualization, Sorrent, Italy*, volume 209, 1998.

[23] Kazuo Ohmi and Hang-Yu Li. Particle-tracking velocimetry with new algorithms. *Measurement Science and Technology*, 11:603–616, 2000.

[24] F Pereira, M Gharib, D Dabiri, and D Modarress. Defocusing digital particle image velocimetry: a 3-component 3-dimensional dpiv measurement technique. application to bubbly flows. *Experiments in Fluids*, 29(1):S078–S084, 2000.

[25] Francisco Pereira, Heinrich Stüer, Emilio C Graff, and Morteza Gharib. Two-frame 3d particle tracking. *Measurement science and technology*, 17(7):1680, 2006.

[26] P Ruhnau, C Guetter, T Putze, and C Schnörr. A variational approach for particle tracking velocimetry. *Measurement Science and Technology*, 16(7):1449, 2005.

[27] A Schröder, R Geisler, K Staack, GE Elsinga, F Scarano, B Wieneke, A Henning, C Poelma, and J Westerweel. Eulerian and lagrangian views of a turbulent boundary layer flow using time-resolved tomographic piv. *Experiments in fluids*, 50(4):1071–1091, 2011.

[28] B Skarman, J Becker, and K Wozniak. Simultaneous 3d-piv and temperature measurements using a new ccd-based holographic interferometer. *Flow Measurement and Instrumentation*, 7(1):1–6, 1996.

[29] Daniele Violato, Peter Moore, and Fulvio Scarano. Lagrangian and eulerian pressure field evaluation of rod-airfoil flow from time-resolved tomographic piv. *Experiments in fluids*, 50(4):1057–1070, 2011.